10.1071/EN20002_AC

Environmental Chemistry 2020, 17(4), 332-344

Supplementary Material

Efficient removal of antimony with natural secondary iron minerals: effect of structural properties and sorption mechanism

Nana Wang,[A] Nairui Deng,[A] Yuyin Qiu,[A] Zebin Su,[A] Chujie Huang,[A] Kaimei Hu,[A] Jianqiao Wang,[A] Liang Ma,[B] Enzong Xiao[A] and Tangfu Xiao[A,C]

[A]Key Laboratory for Water Quality and Conservation of the Pearl River Delta, Ministry of Education, School of Environmental Science and Engineering, Guangzhou University, Guangzhou, 510006, China.

[B]State Key Laboratory of Environmental Geochemistry, Chinese Academy of Sciences, Guiyang, 550081, China.

[C]Corresponding author. Email: tfxiao@gzhu.edu.cn

2.4 Analytical procedures

The microstructures, surface morphologies and elemental compositions of n- and m-SIM were determined using cold field-emission scanning electron microscopy (SEM, SU8220, Hitachi Ltd., Japan) equipped with an energy dispersive X-ray detector (EDS, XFlash 6130, Bruker, Germany). The difference in specific surface areas of n- and m-SIM was determined by N_2 Brunauer–Emmett–Teller (BET) using ASAP 2460 adsorption apparatus (Micromeritics Co., USA). The crystalline structures of SIMs were examined by power X-ray diffraction (XRD, D/max-2500, Rigaku Co., Japan) within the range (2θ) of 5–80° at a scanning rate of 4° min^{-1}. The X-ray photoelectron spectroscope (XPS, Escalab 250Xi, Thermo Fisher Scientific Co., USA) was used to record the surface chemistry properties of SIMs with monochromatic Al Kα radiation. The C1s peak at 284.8 eV was used as the inner standard calibration peak, and a nonlinear least-squares curve-fitting program (XPSPEAK41 Software) was used to process the XPS results. The Fourier transform infrared (FTIR) spectrophotometer (Nicolet 6700, Thermo Fisher Scientific Co., USA) was employed to collect the FTIR spectra of SIMs within the range of 500-4000 cm^{-1}. The Raman spectra of Sb reaction with SIMs were conducted using microconfocal laser Raman spectrometer (LabRAM HR Evolution, Horiba Scientific, USA). The zeta (ζ) potential measurements of SIMs were conducted at different pH values using a zeta potential analyzer (Zetasizer 2000, Malvern, UK) for three times.

The sorption capacities q_e (mg/g) of Sb^{III}/Sb^{V} on n- and m-SIM and removal efficiency R (%) were calculated by the equations:

$$q_e = \frac{(c_0 - c_e)V}{m} \quad (1)$$

$$R = \frac{c_0 - c_e}{c_0} \times 100\% \quad (2)$$

where c_0 and c_e (mg L^{-1}) are the initial and equilibrium concentrations of Sb, respectively; V (mL) is the volume, and m (g) is the mass of SIMs.

3.2.2 Sorption kinetics

To investigate the Sb^{III}/Sb^{V} sorption behaviors of n- and m-SIM, the experimental data were fitted with the pseudo-first-order (PFO) and pseudo-second-order (PSO) models. The PFO kinetic model considers that the sorption rate is dependent on the difference between equilibrium sorption capacity and the sorbed amount, while the PSO kinetic model assumes chemisorption as the rate limiting step, involving valence forces through exchanging or sharing electrons between sorbate and sorbent given below. The linear expressions of these two models are given below (Wang et al., 2016; Yin et al., 2017).

$$\ln(q_e - q_t) = \ln(q_e) - k_1 t \quad (3)$$

$$\frac{t}{q_t} = \frac{1}{k_2 q_e^2} + \frac{1}{q_e} t \quad (4)$$

where q_e and q_t (mg g^{-1}) are the sorption capacities of SIMs at equilibrium and any time t (h), respectively; k_1 (h^{-1}) and k_2 (g $mg^{-1} \cdot h^{-1}$) are the PFO and PSO rate constants, respectively.

3.2.3 Sorption isotherms

The Langmuir isotherm is widely applicable to a homogeneous sorption surface where each active site possesses the identical energy and the sorbate is bound on one site with no transmigration. The Freundlich isotherm is another empirical model

assuming that the multilayer sorption process occurs on a heterogenous surface and sorption energy is not uniformly distributed over the surface (Wang et al., 2016; Zhang et al., 2018). They are expressed in the linear forms:

$$\frac{c_e}{q_e} = \frac{1}{K_L q_m} + \frac{c_e}{q_m} \tag{5}$$

$$\log q_e = \log K_F + \frac{1}{n} \log c_e \tag{6}$$

where c_0 and c_e (mg L^{-1}) are the initial and equilibrium concentration, respectively; q_m (mg g^{-1}) is the maximum Sb^{III}/Sb^{V} sorption capacity, K_L is the Langmuir constant, and K_F (mg g^{-1}) is the sorption capacity coefficient of the Freundlich model, n is the Freundlich constant.

The thermodynamic analysis was used to confirm that the Sb sorption process on n/m-SIM was an endothermic process. The changes in the Gibbs free energy (ΔG°), enthalpy (ΔH°), and entropy (ΔS°) were calculated according to equations (7) and (8) (Luo et al., 2017).

$$\Delta G^{\circ} = -RT\,lnK_L \tag{7}$$

$$lnK_L = \frac{\Delta S^{\circ}}{R} - \frac{\Delta H^{\circ}}{RT} \tag{8}$$

where R is the universal gas law constant (8.314×10^{-3} kJ $mol^{-1} \cdot K^{-1}$), T is the absolute temperature (K), and K_L is the Langmuir adsorption equilibrium constant (L mg^{-1}).

Table S1. The performance comparison between the natural SIMs and various sorbents for Sb^{III}/Sb^{V} removal from water.

sorbents	C_0 (mg L^{-1})		pH		S_{BET}	dosage	sorption capacity (mg g^{-1})		References
	Sb^{III}	Sb^{V}	Sb^{III}	Sb^{V}	(m^2 g^{-1})	(mg L^{-1})	Sb^{III}	Sb^{V}	
δ-MnO_2	0-71	0-55	7.5	7.5	91.9	0.4	2643	158	Sun et al., 2019
triclinic birnessite	0-71	0-55	5.5	7.5	4.6	0.4	169	425	
α-MnO_2 nanofibers	10-500	10-500	6.0	6.0	144	0.5	88-112	84-90	Luo et al., 2017
Fe-Mn binary oxides	-	0.1-150	-	7.0	128-179	0.1	-	146-250	Yang et al., 2018
γ-MnOOH	-	0.5-98.4	-	4-9	-	0.4	-	77-96	Wang et al., 2012
α-FeOOH	0-244	0-244	4-9	4-9	27.4	0.4	43-54	7-25	Guo et al., 2014
β-FeOOH	0-244	0-244	4-9	4-9	32.8	0.4	23-34	11-30	
γ-FeOOH	-	0-244	4-9	4-9	69.6	0.4	-	6-34	
α-Fe_2O_3	0-244	0-244	4-9	4-9	19.9	0.4	25-32	7-24	
HFO	-	0-244	4-9	4-9	152.2	0.4	-	33-114	

Ce-doped Fe_3O_4	10-100	10-100	7.0	7.0	28-152	0.2	111-224	37-188	Qi et al., 2017
Fe-Zr binary oxide	-	0-25	-	7.0	121	0.2	-	51	Li et al., 2012
potassium ferrate	1-10	-	4.0	-		0.05	129.93	-	Lan et al., 201
Schwertmannite granules	0-70.57	0-70.57	7.0	7.0	199.43	1.0	32.9	23.3	Li et al., 2016
Graphene oxide/schwertmannite	-	0-55	-	7.0	287.6	0.3	-	158.6	Dong et al., 2015
Hematite coated magnetic nanoparticle	1-20	-	4.1	-	-	0.1	36.7	-	Shan et al., 2014
Goethite	-	0-244	-	5.5	39.1	4	-	34.1-46.3	Fan et al., 2016
Bentonite	0.05-4	0.05-4	6.0	6.0	-	25	45-68	32-61	Xi et al., 2011
n-SIM	10-300	10-300	7.0	3.0	28.58	0.25	219.78	366.30	This study
m-SIM	10-300	10-300	7.0	3.0	16.91	0.25	160.26	114.94	This study

Table S2. Kinetic parameters for pseudo-first- and pseudo-second-order models for Sb^{III}/Sb^{V} sorption on n-SIM and m-SIM.

sorbents	Kinetic models		PFO			PSO			
	parameters		q_e (mg g^{-1})	K_1 (h^{-1})	R^2	q_e (mg g^{-1})	K_2 (g mg^{-1} h^{-1})	v_0 (mg g^{-1} h^{-1})	R^2
n-SIM	pH=3	Sb^{III}	36.15	0.218	0.947	98.91	0.0361	352.46	0.997
		Sb^{V}	100.12	0.403	0.877	206.19	0.0139	590.95	0.997
	pH=7	Sb^{III}	86.71	0.272	0.987	152.44	0.0112	260.27	0.992
		Sb^{V}	87.53	0.312	0.975	185.87	0.0145	500.94	0.998
m-SIM	pH=3	Sb^{III}	28.13	0.246	0.962	45.35	0.0318	65.40	0.994
		Sb^{V}	45.20	0.232	0.960	66.93	0.0209	93.62	0.994
	pH=7	Sb^{III}	83.14	0.066	0.948	61.61	0.0124	47.07	0.991
		Sb^{V}	36.53	0.299	0.963	60.94	0.0278	103.4	0.996

Table S3. Sorption isotherm parameters of Langmuir and Freundlich models obtained by linear fitting method for Sb^{III}/Sb^{V} sorption on n- and m-SIM.

sorbents		Langmuir			Freundlich		
		q_m (mg g^{-1})	K_L (L mg^{-1})	R^2	K_F (mg g^{-1})	n	R^2
n-SIM Sb^{III}	25°C	189.75	0.0383	0.978	29.782	2.990	0.888
	35°C	206.61	0.0402	0.992	26.103	2.586	0.936
	45°C	219.78	0.0406	0.981	27.867	2.575	0.913
n-SIM Sb^{V}	25°C	331.13	0.1475	1.000	52.010	2.543	0.580
	35°C	352.11	0.1569	0.999	60.813	2.703	0.570
	45°C	366.30	0.1496	0.999	62.997	2.717	0.513
m-SIM Sb^{III}	25°C	143.47	0.0291	0.984	17.611	2.679	0.942
	35°C	155.04	0.0349	0.990	20.160	2.698	0.939
	45°C	160.26	0.0443	0.991	27.683	3.119	0.932
m-SIM Sb^{V}	25°C	70.27	0.0416	0.990	9.794	2.705	0.637
	35°C	99.60	0.0398	0.991	13.330	2.681	0.851
	45°C	114.94	0.0423	0.995	14.628	2.550	0.875

Table S4. Thermodynamic parameters of Sb^{III}/Sb^{V} sorption on n- and m-SIM at different temperatures.

	Sb^{III}			Sb^{V}		
	T (K)	$\ln K_L$	ΔG (kJ mol^{-1})	T (K)	$\ln K_L$	ΔG (kJ mol^{-1})
n-SIM	298	3.645	-9.032	298	4.994	-12.373
	308	3.689	-9.446	308	5.056	-12.946
	318	3.704	-9.792	318	5.008	-13.240
	$\Delta H°$ (kJ mol^{-1})		2.309	$\Delta H°$ (kJ mol^{-1})		0.603
	$\Delta S°$ (kJ $mol^{-1}\cdot K^{-1}$)		0.038	$\Delta S°$ (kJ $mol^{-1}\cdot K^{-1}$)		0.044
m-SIM	298	3.371	-8.351	298	3.728	-9.237
	308	3.552	-9.097	308	3.684	-9.433
	318	3.791	-10.023	318	3.745	-9.901
	$\Delta H°$ (kJ mol^{-1})		16.525	$\Delta H°$ (kJ mol^{-1})		0.612
	$\Delta S°$ (kJ $mol\cdot K^{-1}$)		0.084	$\Delta S°$ (kJ $mol^{-1}\cdot K^{-1}$)		0.033

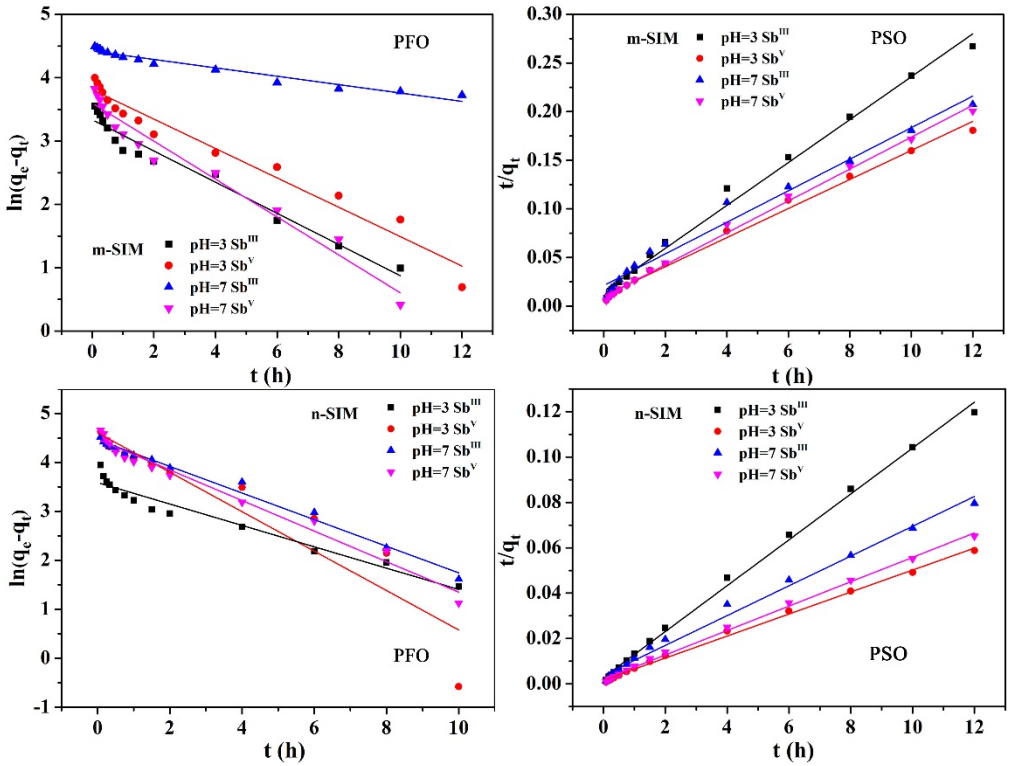

Fig. S1 Kinetics for Sb^{III} and Sb^{V} sorption on n- and m-SIM at pH 3.0 and 7.0: PFO and PSO models.

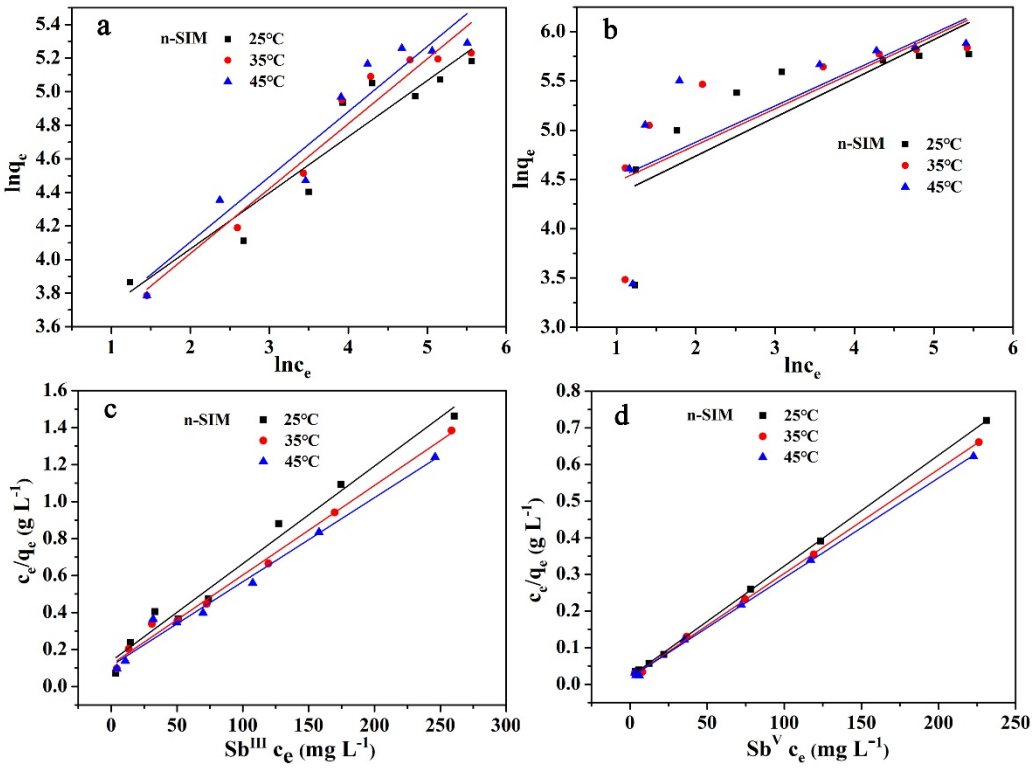

Fig. S2 Isotherms for Sb^{III} (a, c) and Sb^{V} (b, d) sorption on n-SIM: (a, b) Freundlich and (c, d) Langmuir.

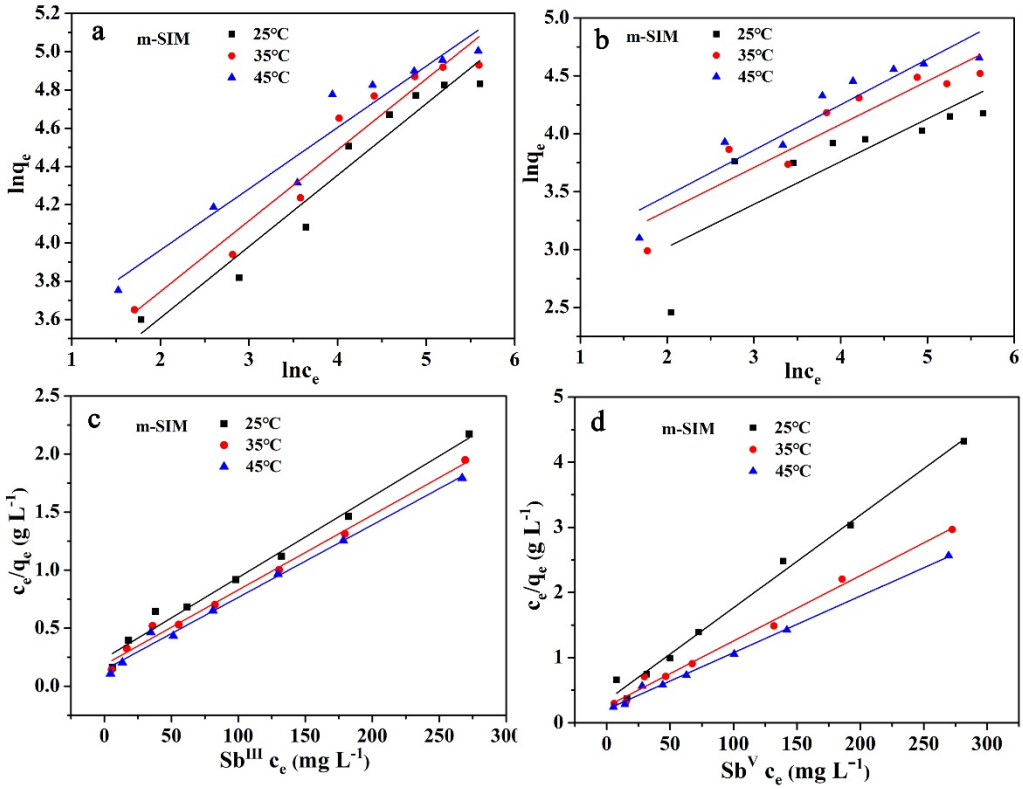

Fig. S3 Isotherms for Sb^{III} (a, c) and Sb^{V} (b, d) sorption on m-SIM: (a, b) Freundlich and (c, d) Langmuir.

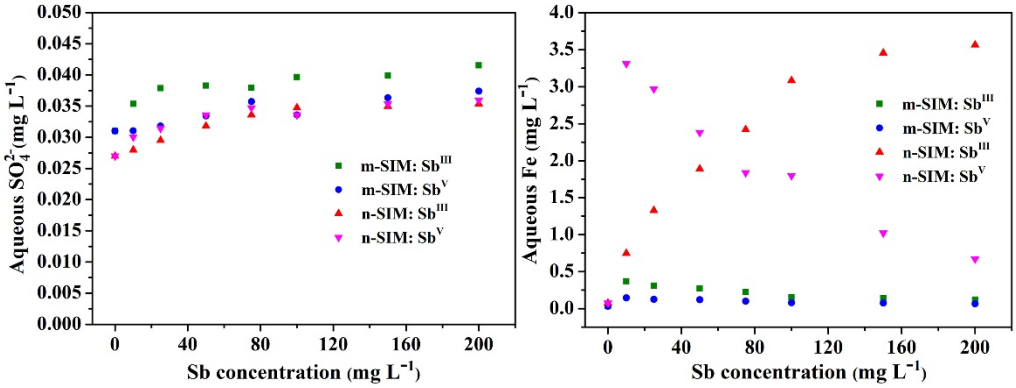

Fig. S4 $Fe_{(aq)}$ and SO_4^{2-} concentrations in the aqueous solution after Sb^{III}/Sb^{V} sorption onto n- and m-SIMs (the points at an Sb concentration of 0 mg L^{-1} refer to the control experimental results, pH =7.0 for Sb^{III} and 3.0 for Sb^{V})

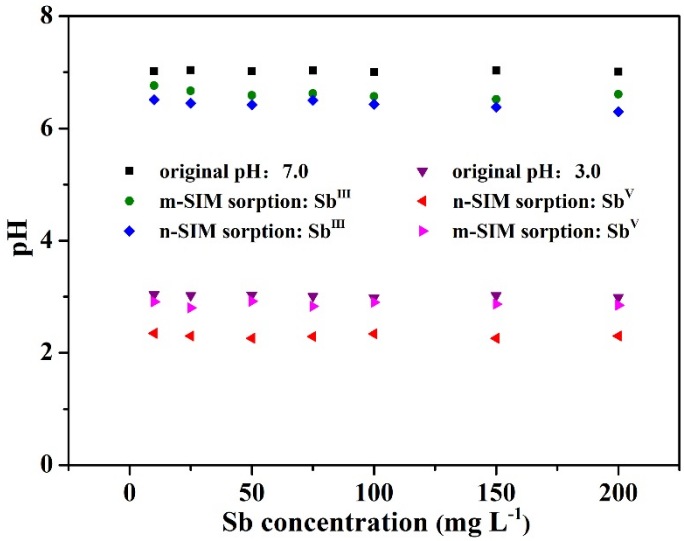

Fig. S5 pH evolution of the aqueous solution after Sb^{III}/Sb^{V} sorption onto n- and m-SIM.

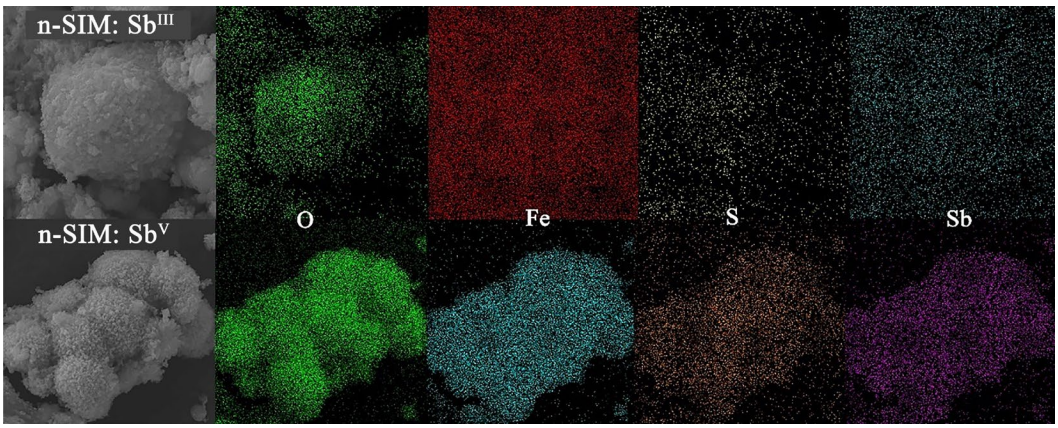

Fig. S6 The mapping images of n-SIM after Sb^{III}/Sb^{V} sorption.

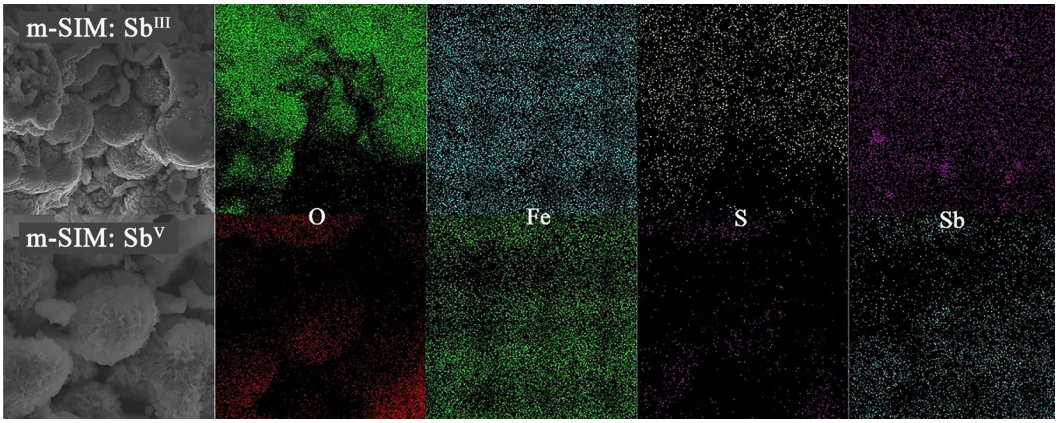

Fig. S7 The mapping images of m-SIM after Sb^{III}/Sb^{V} sorption.

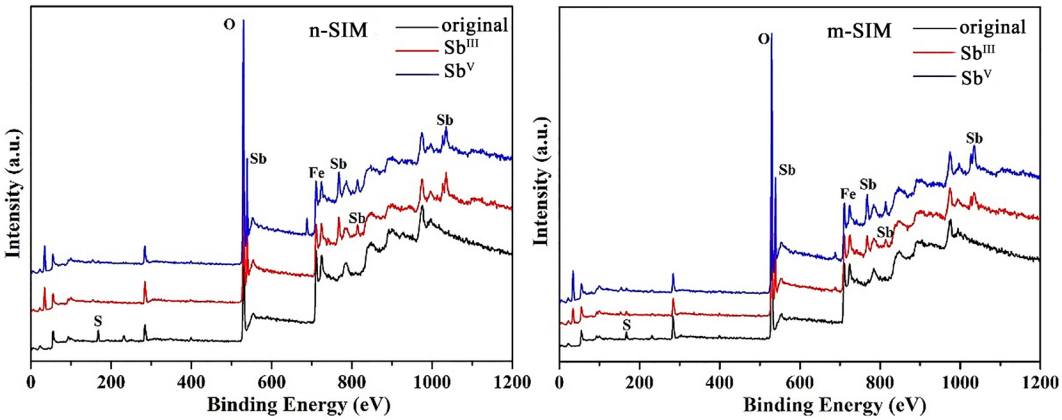

Fig. S8 XPS spectra of n- and m-SIM before and after Sb^{III}/Sb^{V} sorption.

References

Dong, S., Dou, X., Mohan, D., Pittman, C.U., Luo, J. (2015). Synthesis of graphene oxide/schwertmannite nanocomposites and their application in Sb(V) adsorption from water. *Chemical Engineering Journal* **270**, 205-214. DOI: 10.1016/j.cej.2015.01.071.

Fan, J.-X., Wang, Y.-J., Fan, T.-T., Dang, F., Zhou, D.-M. (2016). Effect of aqueous Fe(II) on Sb(V) sorption on soil and goethite. *Chemosphere* **147**, 44-51. DOI: 10.1016/j.chemosphere.2015.12.078.

Guo, X., Wu, Z., He, M., Meng, X., Jin, X., Qiu, N., Zhang, J. (2014). Adsorption of antimony onto iron oxyhydroxides: Adsorption behavior and surface structure. *Journal of Hazardous Materials* **276**, 339-345. DOI: 10.1016/j.jhazmat.2014.05.025.

Lan, B., Wang, Y., Wang, X., Zhou, X., Kang, Y., Li, L. (2016). Aqueous arsenic (As) and antimony (Sb) removal by potassium ferrate. *Chemical Engineering Journal* **292**, 389-397. DOI: 10.1016/j.cej.2016.02.019.

Li, X., Dou, X., Li, J. (2012). Antimony(V) removal from water by iron-zirconium bimetal oxide: Performance and mechanism. *Journal Environmental Sciences* **24**, 1197-1203. DOI: 10.1016/s1001-0742(11)60932-7.

Li, Y., Mohan, D., Pittman, C.U., Ok, Y.S., Dou, X. (2016). Removal of antimonate and antimonite from water by schwertmannite granules. *Desalination and Water Treatment* **57**, 25639-25652. DOI: 10.1080/19443994.2016.1155176.

Luo, J., Hu, C., Meng, X., Crittenden, J., Qu, J., Peng, P. (2017). Antimony removal from aqueous solution using novel α-MnO_2 nanofibers: Equilibrium, kinetic, and density functional theory studies. *ACS Sustainable Chemistry & Engineering* **5**, 2255-2264. DOI:

10.1021/acssuschemeng.6b02583.

Qi, Z., Joshi, T.P., Liu, R., Liu, H., Qu, J. (2017). Synthesis of Ce(III)-doped Fe_3O_4 magnetic particles for efficient removal of antimony from aqueous solution. *Journal of Hazardous Materials* **329**, 193-204. DOI: 10.1016/j.jhazmat.2017.01.007.

Shan, C., Ma, Z., Tong, M. (2014). Efficient removal of trace antimony(III) through adsorption by hematite modified magnetic nanoparticles. *Journal of Hazardous Materials* **268**, 229-236. DOI: 10.1016/j.jhazmat.2014.01.020.

Sun, Q., Cui, P.-X., Liu, C., Peng, S.-M., Alves, M.E., Zhou, D.-M., Shi, Z.-Q., Wang, Y.-J. (2019). Antimony oxidation and sorption behavior on birnessites with different properties (δ-MnO_2 and triclinic birnessite). *Environmental Pollution* **246**, 990-998. DOI: 10.1016/j.envpol.2018.12.027.

Wang, N., Xu, X., Li, H., Zhai, J., Yuan, L., Zhang, K., Yu, H. (2016). Preparation and application of a xanthate-modified thiourea chitosan sponge for the removal of Pb(II) from aqueous solutions. *Industrial & Engineering Chemistry Research* **55**, 4960-4968. DOI: 10.1021/acs.iecr.6b00694.

Wang, X., He, M., Lin, C., Gao, Y., Zheng, L. (2012). Antimony(III) oxidation and antimony(V) adsorption reactions on synthetic manganite. *Chemie der Erde - Geochemistry* **72**, 41-47. DOI: 10.1016/j.chemer.2012.02.002.

Xi, J., He, M., Lin, C. (2011). Adsorption of antimony(III) and antimony(V) on bentonite: Kinetics, thermodynamics and anion competition. *Microchemical Journal* **97**, 85-91. DOI: 10.1016/j.microc.2010.05.017.

Yang, K., Zhou, J., Lou, Z., Zhou, X., Liu, Y., Li, Y., Ali Baig, S., Xu, X. (2018). Removal of Sb(V)

from aqueous solutions using Fe-Mn binary oxides: The influence of iron oxides forms and the role of manganese oxides. *Chemical Engineering Journal* **354**, 577-588. DOI: 10.1016/j.cej.2018.08.069.

Yin, L., Wang, P., Wen, T., Yu, S., Wang, X., Hayat, T., Alsaedi, A., Wang, X. (2017). Synthesis of layered titanate nanowires at low temperature and their application in efficient removal of U(VI). *Environmental Pollution* **226**, 125-134. DOI: 10.1016/j.envpol.2017.03.078.

Zhang, G., Fan, F., Li, X., Qi, J., Chen, Y. (2018). Superior adsorption of thallium(I) on titanium peroxide: Performance and mechanism. *Chemical Engineering Journal* **331**, 471-479. DOI: 10.1016/j.cej.2017.08.053.